Mechanism of Zn Insertion into Nanostructured δ-MnO$_2$: A Nonaqueous Rechargeable Zn Metal Battery

Sang-Don Han,[*,†,‡] Soojeong Kim,[†,‡] Dongguo Li,[§] Valeri Petkov,[#] Hyun Deog Yoo,[†,‖]
Patrick J. Phillips,[†,⊥] Hao Wang,[†,‡] Jae Jin Kim,[‡] Karren L. More,[¶] Baris Key,[†,‡] Robert F. Klie,[†,⊥]
Jordi Cabana,[†,‖] Vojislav R. Stamenkovic,[§] Timothy T. Fister,[†,‡] Nenad M. Markovic,[†,§]
Anthony K. Burrell,[†,‡] Sanja Tepavcevic,[*,†,§] and John T. Vaughey[*,†,‡]

[†]Joint Center for Energy Storage Research (JCESR), [‡]Chemical Sciences and Engineering Division, and [§]Material Science Division,
Argonne National Laboratory, Argonne, Illinois 60439, United States
[#]Department of Physics, Central Michigan University, Mt. Pleasant, Michigan 48859, United States
[‖]Department of Chemistry and [⊥]Department of Physics, University of Illinois at Chicago, Chicago, Illinois 60607, United States
[¶]Center for Nanophase Materials Sciences, Oak Ridge National Laboratory, Oak Ridge, Tennessee 37831, United States

S Supporting Information

ABSTRACT: Unlike the more established lithium-ion based energy storage chemistries, the complex intercalation chemistry of multivalent cations in a host lattice is not well understood, especially the relationship between the intercalating species solution chemistry and the prevalence and type of side reactions. Among multivalent metals, a promising model system can be based on nonaqueous Zn^{2+} ion chemistry. Several examples of these systems support the use of a Zn metal anode, and reversible intercalation cathodes have been reported. This study utilizes a combination of analytical tools to probe the chemistry of a nanostructured δ-MnO$_2$ cathode in association with a nonaqueous acetonitrile−Zn(TFSI)$_2$ electrolyte and a Zn metal anode. As many of the issues related to understanding a multivalent battery relate to the electrolyte−electrode interface, the high surface area of a nanostructured cathode provides a significant interface between the electrolyte and cathode host that maximizes the spectroscopic signal of any side reactions or minor mechanistic pathways. Numerous factors affecting capacity fade and issues associated with the second phase formation including Mn dissolution in heavily cycled Zn/δ-MnO$_2$ cells are presented including dramatic mechanistic differences in the storage mechanism of this couple when compared to similar aqueous electrolytes are noted.
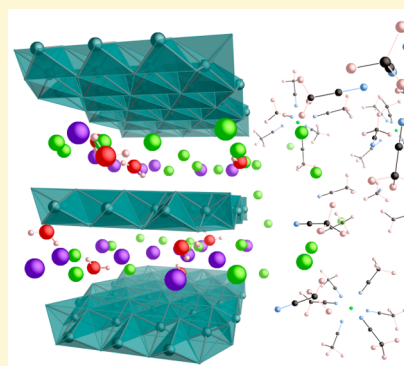
The quest for new energy storage technologies for transportation applications is rapidly moving toward high performance, safe, and low cost technologies. Recently, nonaqueous multivalent metal (e.g., Mg, Zn, Ca, and Al) based cells have drawn attention from numerous research groups as a promising advanced energy storage technology due to their higher theoretical volumetric capacity, limited dendrite formation, and lower materials cost. A major obstacle for multivalent systems, however, is the identification of electrolytes that show reversible deposition/dissolution on a metal anode and support reversible intercalation of multivalent ions into a cathode.[1,2] In the case of nonaqueous Mg or Ca ion systems the electrolyte compatibility issues (e.g., low Coulombic efficiency, a high overpotential, and corrosion) with electrodes and current collectors have held back the development of these systems.[3] Recently developed non-corrosive halogen-free Mg electrolyte is compatible with Mg metal and possesses high anodic stability, which possibly accelerates the research and development of high-voltage cathodes.[4] However, nonaqueous Zn^{2+} ion chemistry with a reversible intercalation cathode is an exception among

multivalent metals with several promising features including highly efficient reversible Zn deposition behavior on a Zn metal anode with a wide electrochemical window,[3] relatively lower activation barrier energy for diffusion in several cathode materials (e.g., NiO$_2$, V$_2$O$_5$, and FePO$_4$),[5] a similar ionic radius to Li$^+$ and Mg^{2+} ions,[6] and high volumetric capacity.[1] Considering these intrinsic properties, a nonaqueous Zn system provides an opportunity to delve into the mechanisms of a multivalent-ion based electrochemical cell and develop a better understanding of the interactions between the electrode, solvated species, and electrolyte.

Recently developed nonaqueous Zn(II) electrolytes show reversible electrodeposition on a Zn metal anode (≥99% of Coulombic efficiency) and provide wide electrochemical window (up to ∼3.8 V vs Zn/Zn^{2+} vs a Pt electrode).[3] At the same time, oxide cathode materials that have intrinsically higher voltages (with respect to more commonly studied

sulfides) show no activity or a limited amount of multivalent ion intercalation with decomposition to secondary phases (via an irreversible conversion reactions and/or second phase formation) open noted.[7,8] As reported in previous studies,[9−13] design strategies, including nanosizing or incorporation of solvent molecules into host crystalline structure (to facilitate effective charge screening) were required to enable multivalent ion intercalation into oxides hosts. Additional computational studies have suggested that the multivalent migration energy in the layered structures is lower than in other three-dimensional structures (e.g., spinel and olivine).[5] Previous chemical intercalation studies (i.e., Zn^{2+} ion intercalation into the layered compound WO_2Cl_2)[14] along with recent electrochemical cycling results for the nonaqueous Zn/layered V_2O_5,[15] aqueous Zn/layered MnO_2,[16] and aqueous/nonaqueous Mg/layered MnO_2[17,18] cells have demonstrated reasonable cycling performances. In this study, based on the above design strategies and experimental results, a nanostructured $K_{0.11}MnO_2\cdot0.7H_2O$ (layered birnessite, labeled δ-MnO_2) cathode material with crystallographically bonded water molecules was synthesized using a low temperature water-based synthetic route. This material was chosen as a model system because previous studies had highlighted the role of the electrolyte in its energy storage mechanism, specifically that using an aqueous Zn electrolyte led to a gradual conversion to a three-dimensional spinel structure.[16]

Several previous studies have demonstrated different cycling performances and insertion mechanisms of multivalent ions into δ-MnO_2 host material in aqueous/nonaqueous electrolytes. Studies of hydrated δ-MnO_2 cathodes in both aqueous and (wet) nonaqueous electrolytes have revealed the crucial role of the crystallographic water in the host material and its importance in lowering the desolvation energy penalty at the cathode–electrolyte interface.[17] A recent investigation of a structurally quasi-reversible Mg^{2+} ion insertion mechanism in a nanostructured δ-MnO_2 cathode, performed using nonaqueous and aqueous electrolytes, indicated energy storage occurs in the nonaqueous electrolyte with the formation of MnOOH, MnO, and $Mg(OH)_2$, while the intercalation of Mg^{2+} ions takes place with transformation to a spinel-like phase.[18] However, a δ-MnO_2 nanoscale cathode cell with an aqueous 1.0 M $ZnSO_4$ (pH 4.0) electrolyte yielded capacities as high as ~240 mAh g^{-1} at a current density of 83 mA g^{-1} with a Coulombic efficiency of ≥99% for 100 cycles.[16] As with the Mg^{2+} system, electrode degradation was also observed with a structural transformation from the layered δ-MnO_2 to spinel $ZnMn_2O_4$. Another recent study reported the intercalation of Zn ions into an α-MnO_2 (a one-dimensional tunnel structure) cathode in an aqueous 1.0 M $ZnSO_4$ electrolyte.[19] It was noted that during the discharge–charge reactions of these Zn-ion batteries a reversible phase transition of the MnO_2 cathode from the one-dimensional tunnel of α-MnO_2 to layered birnessite-like (δ-MnO_2) polymorphs was driven by electrochemical reactions. Combined with a metal anode, understanding the underlying intercalation mechanism of these aqueous systems and adapting them to nonaqueous systems in a multivalent metal cell and the underlying principles behind reversible intercalation of multivalent ions into a cathode (e.g., intercalation vs conversion and possible structural transformation compared to an aqueous system) is a valuable asset for multivalent cell design.

In this study, the cycling performance of a Zn/δ-MnO_2 cell and related Zn^{2+} ion insertion chemistry on the δ-MnO_2 host material have been investigated in the recently developed nonaqueous acetonitrile(AN)−Zn(TFSI)$_2$ electrolyte. A Zn/δ-MnO_2 cell demonstrates good reversibility (>99% Coulombic efficiency) and stability for 125 cycles with capacities as high as 123 mAh g^{-1} (at a current density of 12.3 mA g^{-1}) and an operating voltage of 1.25 V (vs Zn/Zn^{2+}). The detailed fundamental study focuses on the electrochemical Zn^{2+} ion insertion mechanism in a nonaqueous electrolyte and the factors that lead to capacity fade in an effort to understand the key parameters underpinning the development of multivalent metal batteries, especially when compared to the more common aqueous-based systems.

■ EXPERIMENTAL SECTION

Synthesis. Appropriate ratios of dried zinc(II) bis(trifluoromethanesulfonyl)imide salt (Zn(TFSI)$_2$, Solvionic, 99.5%) and dried anhydrous acetonitrile solvent (AN, Sigma-Aldrich, 99.8%) were mixed together in hermetically sealed glass vials and stirred on a stirring plate to form homogeneous solutions.[3] All materials were handled in an argon-filled inert atmosphere glovebox (<0.5 ppm of H_2O and <0.5 ppm of O_2). The water content of the mixtures was confirmed to be <30 ppm using a Mettler Toledo DL39 Karl Fischer coulometer.

To synthesize nanostructured low crystalline δ-MnO_2 powder potassium permanganate (KMnO$_4$, ACS reagent, ≥99.0%) and manganese sulfate monohydrate (MnSO$_4\cdot$H$_2$O, ACS reagent, ≥98%) were purchased from Sigma-Aldrich and used without further purification. Potassium permanganate (2.5 mmol) and manganese sulfate monohydrate (1.0 mmol) were added into a three-necked flask, and 30 mL of milli-Q water (18.2 MΩ·cm) was added to form a purple solution under stirring at 400 rpm. The solution was refluxed for 2 h in air. The manganese oxide precipitate was washed by milli-Q water and collected by centrifugation (8500 rpm for 5 min). The powder was dried in air at room temperature. Note that colloidal synthesis of nanostructured materials is often conducted in the presence of capping agent. In our case, no surfactant was added during the synthesis, which avoids additional surfactant removal procedure and possible structural changes of manganese oxide.[20] The ideal reaction mechanism in the synthesis is

$$2KMnO_4 + 2MnSO_4 + H_2O \rightarrow 4MnO_x + K_2SO_4 + H_2SO_4$$
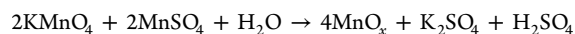
The molar ratio between the KMnO$_4$ and MnSO$_4$ precursors determine the oxidation state of Mn (between Mn(III) and Mn(IV)) in the manganese oxide product. Elemental analysis confirmed that nanostructured $K_{0.11}MnO_2\cdot0.7H_2O$ (22% of Mn(II) and 78% of Mn(IV) for the MnO_2) was synthesized. The slurry for the coating was prepared by mixing a 8:1:1 ratio by weighing of dried δ-MnO_2 powder (75 °C under vacuum overnight), Super C45 carbon black (Timcal), and Solef polyvinylidene difluoride (Solvay) with n-methyl-2-pyrrolidinone (anhydrous, Sigma-Aldrich). Electrodes were then coated onto the carbon coated aluminum foil (18 μm thick, MTI Corporation) using a doctor blade of approximately 100 μm, and subsequently dried in a 75 °C vacuum oven overnight followed by further drying 2−3 h in a 90 °C vacuum oven placed in an argon-filled inert atmosphere glovebox. The loading of δ-MnO_2 on the electrode was 1.5–2.0 mg cm^{-2} (0.97 cm^2 of surface area).

Electrochemistry. Galvanostatic cycling measurements on δ-MnO_2 electrodes were carried out using 2032 coin-type cells, which are assembled in an argon-filled inert atmosphere glovebox (<0.5 ppm of H_2O and <0.5 ppm of O_2). The cells were built using δ-MnO_2 cathode and Zn metal anode and separated by a Whatmann glass fiber separator soaked in the 0.5 M AN−Zn(TFSI)$_2$ electrolyte. Cycling was carried out in a Maccor series 4400 battery tester between 0.05 and 1.9 V vs Zn^{2+}/Zn as voltage window at C/25 rate (i.e., 12.3 mA g^{-1}) and at room temperature.

The electrochemical impedance spectroscopy (EIS) was measured at frequencies from 100 kHz to 8 mHz, amplitude voltage of 10 mV using a Solartron 1260 Multistat impedance analyzer. The obtained spectra was evaluated by complex nonlinear least-squares (CNLS)
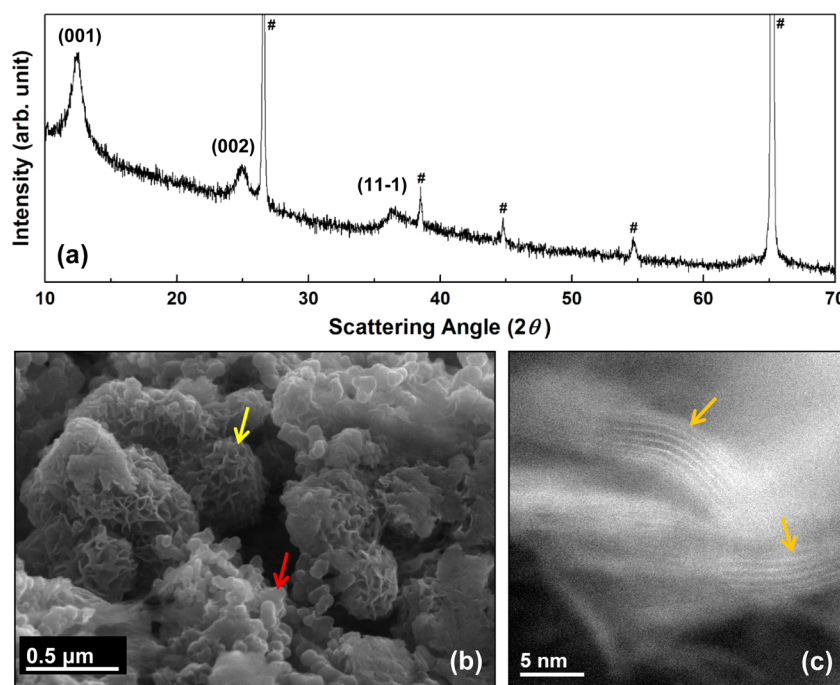
Figure 1. (a) XRD pattern (#, carbon-coated Al as a current collector), (b) SEM images (yellow arrow, δ-MnO₂ floret-like particles; red arrow, carbon black particles), and (c) HAADF-STEM images (orange arrows, layered structures) of δ-MnO₂.

fitting with ZView2 software (Scribner Associates Inc.) based on equivalent circuits.

Characterization. X-ray powder diffraction (XRD) analysis for the samples was performed using a Rigaku MiniFlex 600 (Cu Kα radiation) from 10° to 80° (2θ) with step size of 0.01°.

High-angle annular dark field (HAADF) high-resolution scanning transmission electron microscopy (HR-STEM) and energy-dispersive spectroscopy (EDS) were performed using an aberration-corrected JEOL 2200FS STEM to analyze the as-synthesized electrode material.

X-ray absorption near-edge structure (XANES) and X-ray absorption fine structure (XAFS) measurements were performed at sector 10BM at the Advanced Photon Source.[21] X-ray absorption spectra were collected in transmission mode through the δ-MnO₂ electrodes. A Mn metal reference foil was measured simultaneously with each sample for energy calibration, with the metal K-edge set to 6539 eV. All samples were sealed in aluminized mylar to prevent air exposure. Data were analyzed using the *IFEFFIT* package.[22,23]

Magic angle spinning (MAS) ¹H nuclear magnetic resonance (NMR) spectra were collected for the completely dried as-synthesized α-MnO₂ powder and the pristine, discharged, and charged δ-MnO₂ electrodes. A magnetic field strength of 7.03 T was used in these experiments with a Bruker spectrometer and 1.3 mm HX probe, and the samples were spun at 60 kHz at 283 K. The ¹H NMR spectra were acquired with rotor synchronized spin−echo experiments ($90°−τ−180°−τ$) where $τ = n/νr$ ($νr$: spinning speed in Hz), and a $π/2$ of 1.4 μs was used. Samples were packed into a 1.3 mm rotor under inert atmosphere, and a total of 256 scans were accumulated for each sample.

High-energy X-ray diffraction (HE-XRD) experiments were carried out at the 11-ID-C beamline at the Advanced Photon Source, Argonne National Laboratory using X-rays with wavelength of $λ = 0.1080$ Å. Samples were measured in transmission geometry and scattered X-ray intensities collected with a large area 2D detector. Experimental HE-XRD patterns were reduced to the atomic pair distribution functions (PDFs) following well-established procedures.[24] Note atomic PDFs $G(r)$ are experimental quantities that oscillate around zero and show positive peaks at real space distances, r, where the local atomic density $ρ(r)$ exceeds the average one $ρ_o$. This behavior can be expressed by the equation $G(r) = 4πrρ_o[ρ(r)/ρ_o − 1]$, which is the formal definition of the PDF $G(r)$. Here $ρ(r)$ and $ρ_o$ are the local and average atomic

number density, respectively. HE-XRD and atomic PDFs have already proven to be efficient in studying the atomic-scale structure of intrinsically disordered materials, including materials used as cathodes and anodes in batteries.[25−27]

All scanning transmission electron microscopy (STEM) imaging and energy-dispersive X-ray (EDX) spectroscopy were performed on an aberration-corrected JEOL JEM-ARM200CF operated at 80 kV. Images were acquired in high-angle annular dark field (HAADF) mode, such that the resulting imaging contrast is approximately Z∧2. The ARM200CF is equipped with an Oxford X-Max 100TLE windowless silicon drift EDX detector.

Determination of Mn concentrations from the cycled separator was accomplished by inductively coupled plasma mass spectrometry (ICP-MS) analysis (PerkinElmer NexION 300D). The solution matrix consisted of 1% HNO_3 with the addition of 1% acetonitrile. Samples were prepared by diluting at a 1:100 ratio with dimethyl carbonate solution. Due to the presence of the organic species, the analysis was run using Kinetic Energy Discrimination (KED) mode, with He flow rate at 3.8 mL min⁻¹. Plasma parameters were set to 1600 W RF power, 15.6 Lpm Ar plasma flow rate, and 1.2 Lpm Ar auxiliary gas. A Meinhard nebulizer was used to introduce the sample with 1 Lpm Ar as nebulizer gas and a cyclonic spray chamber. Mn concentration was measured using signal from mass-to-charge ratios of 55. Sc was used as an internal standard.

■ RESULTS AND DISCUSSION

Materials Characterization. As shown in previous studies,[3] the 0.5 M AN−Zn(TFSI)₂ electrolyte demonstrates highly reversible Zn deposition behavior on a Zn metal anode (≥99% of Coulombic efficiency) and displays high anodic stability (∼3.6 V vs Zn/Zn²⁺ vs a Pt electrode). Such a large window of stability for the electrolyte within the nonaqueous Zn(II) electrolyte system allows for the study and evaluation of several high voltage oxide-based cathodes, including the couple Zn/δ-MnO₂.

The (001) peak at 12.5° is characteristic of the ∼7 Å spacing in the layered δ-MnO₂ material (Figure 1a). The spacing is due to structural water in the interlayer gap.[18,28,29] The amount of
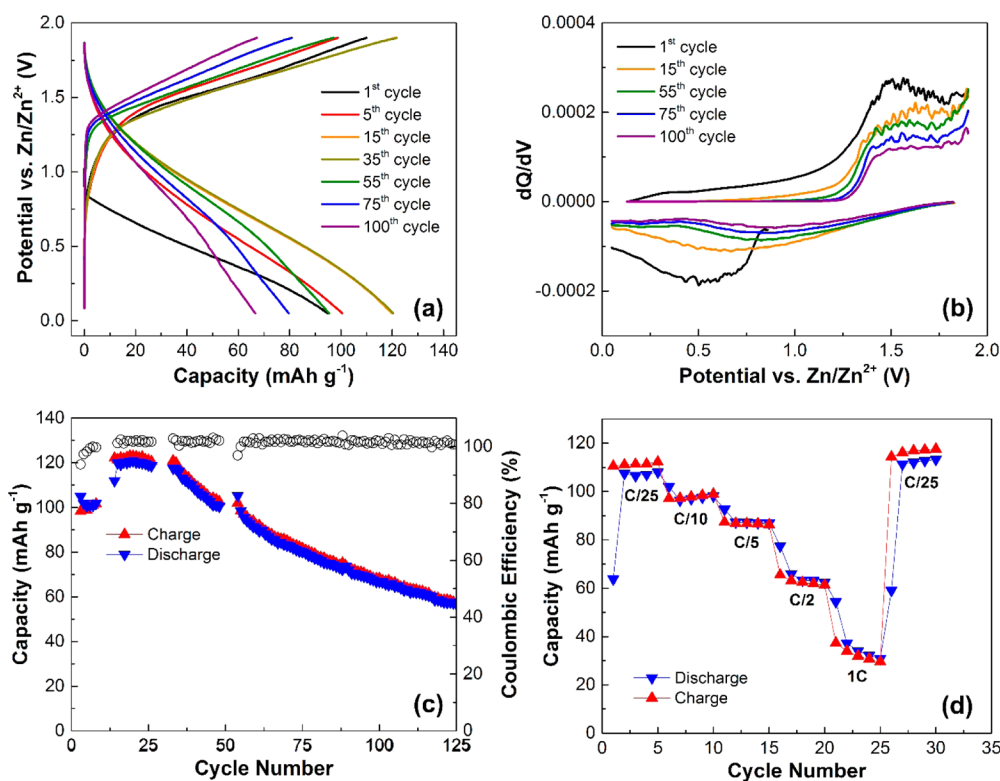
Figure 2. (a) Potential vs capacity profiles, (b) corresponding dQ/dV curves, and (c) capacity vs cycle number profiles of the Zn/δ-MnO$_2$ cells at C/25 C-rates. (d) Capacity vs cycle number profiles of the Zn/δ-MnO$_2$ cells at different C-rates.

water was determined by TGA to be ~0.7 mol of (bound) H$_2$O per mol of a vacuum-dried δ-MnO$_2$ (Figure S1). The relatively broad diffraction peaks are in good agreement with the nanostructured δ-MnO$_2$ observed by electron microscopy (Figure 1c). The observed morphology of the as-synthesized δ-MnO$_2$ particles is a floret-like structure formed by growth of intersecting flakes of layered δ-MnO$_2$ (Figure 1b). The diameter of typical floret-like δ-MnO$_2$ particles (yellow arrow in Figure 1b) is 0.2−0.5 μm, which are surrounded by carbon black particles (red arrow in Figure 1b). The high-angle dark-field imaging (HAADF) STEM analysis (Figure 1c) shows that the total thickness of δ-MnO$_2$ flakes ranged from 5 to 15 stacked (001) planes. The thickness of each interlayer of stacked planes is measured as ~7 Å, which is consistent with d = 7.3 Å for the (001) planes of layered δ-MnO$_2$.[18]

In general, δ-MnO$_2$ is built from layers of distorted MnO$_6$ octahedra that, due to their low temperature synthesis, display irregular spacing, turbostratic disorder, and random Mn vacancies.[28] To compensate the unbalanced local charge on the layers the interlayer space is typically filled with a foreign species, such as hydrated K$^+$ ions.[29,30] These various degrees of disorder combined with random cation vacancies yield a commonly accepted structural model of δ-MnO$_2$ that lacks specificity due to the extent defects tolerated by the material. The average oxidation state of Mn in the as-synthesized δ-MnO$_2$ is slightly lower than tetravalent. These conclusions are consistent with the PDF analysis that has indicated that the as-synthesized δ-MnO$_2$ is distorted structurally with average Mn−O bonds lengths around 1.9 ($\pm$ 0.1) Å, consistent with reported values (Figure S2).[31,32]

Electrochemistry. *Potential Profiles.* To demonstrate the feasibility of Zn^{2+} insertion into a synthesized δ-MnO$_2$ cathode and its compatibility with 0.5 M AN−Zn(TFSI)$_2$ electrolyte,

coin-type cells were fabricated against Zn metal and cycled at a current density of C/25 (12.3 mA g^{-1}) over the potential range of 0.05−1.9 V vs Zn^{2+}/Zn. Figure 2a,b represents variable capacities with respect to potentials and their corresponding derivative profiles (i.e., dQ/dV curves) for a Zn/δ-MnO$_2$ cell. The open circuit voltage (OCV) of the Zn/δ-MnO$_2$ cell is ~1.0 V vs Zn^{2+}/Zn. Upon the first discharge the potential of the cell sharply decreased to ~0.9 V vs Zn^{2+}/Zn and then gradually decreased to 0.05 V vs Zn^{2+}/Zn with a total capacity of approximately 95 mAh g^{-1}, while upon subsequent charge of the cell the potential abruptly increased to ~0.8 V vs Zn^{2+}/Zn and then smoothly increased to 1.9 V vs Zn^{2+}/Zn with a corresponding capacity of approximately 110 mAh g^{-1} (Figure 2a). In the first cycle, the difference between discharge and charge capacity values is possibly attributable to slight compositional changes (e.g., K dissolution) and/or electrolyte decomposition. The following cycles show similar discharge and charge capacity values. It is noted that the average potential of the cell increases from 1.25 to 1.37 V vs Zn^{2+}/Zn, which has been ascribed to possible structural changes of a host material. If the observed capacities are ascribed to processes involving Zn^{2+} ion insertion and deinsertion, the highest value observed capacity (i.e., 123 mAh g^{-1}) corresponds to approximately 0.2 mol of Zn^{2+} ions inserted per mole of MnO$_2$. The corresponding dQ/dV curves of the Zn/δ-MnO$_2$ cell demonstrate evolving voltage features on cycling (Figure 2b). For the first cycle, there is one broad peak at ~0.5 V vs Zn^{2+}/Zn on reduction and correspondingly another broad peak at ~1.5 V vs Zn^{2+}/Zn on oxidation. As the cell cycles, the ~1.5 V oxidation peak remains but decreases in intensity, while the reduction peak at ~0.5 V vs Zn^{2+}/Zn drifts to slightly higher voltage (~0.85 V vs Zn^{2+}/Zn) and also diminishes in intensity. These changes in voltage profiles and dQ/dV curves (Figure
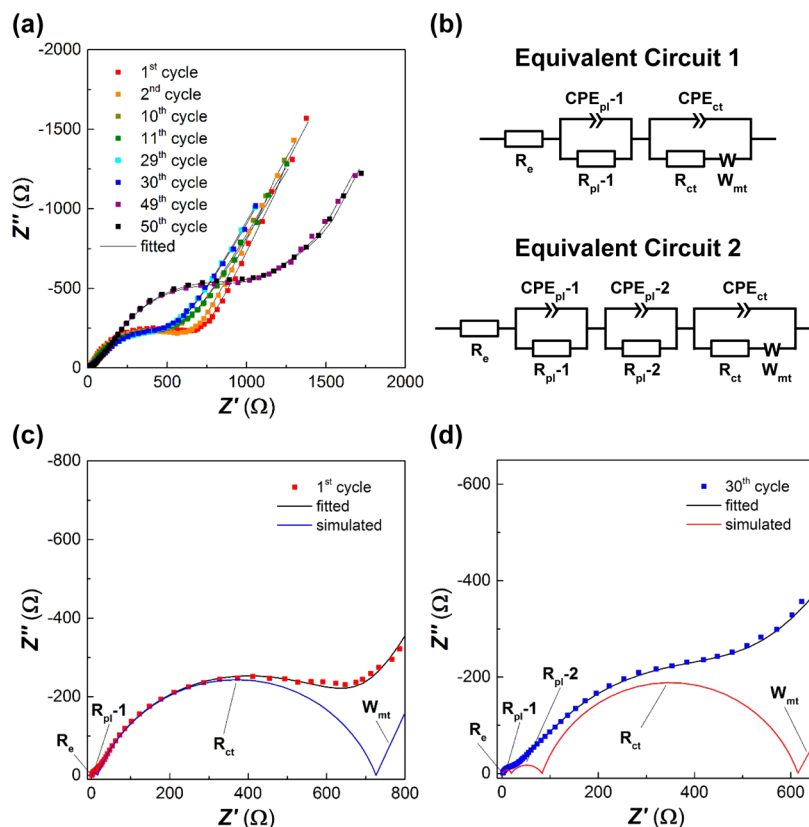
Figure 3. (a) Electrochemical impedance spectra of the Zn/δ-MnO$_2$ cells obtained at different cycling points (at C/25 C-rate). (b) Corresponding equivalent circuits that were used for the fitting. Magnified views of the fitted impedance spectra for (c) the 1st cycle and (d) the 30th cycle based on the equivalent circuits from panel b.

2a,b) have been attributed to a combination of factors, including electrochemical grinding, structural rearrangement, exchange of solvent molecules from the electrolyte, or electrolyte decomposition.[33−35] Figure 2c shows typical long-term cycling performance with ≥99% Coulombic efficiency for the Zn/δ-MnO$_2$ cell. It is noted that the capacity increased to 123 mAh g^{-1} after the 20th cycle before the initiation of capacity fade, a conditioning process that was also observed in Mg/δ-MnO$_2$ systems.[18] It has been suggested that this process is attributable to improved electrode wetting on cycling with increasing electronic contact of the nanosized active materials. After the 30th cycle, the capacity decreases gradually. This has been attributed to several factors including severe electrolyte decomposition, slow loss of electronic contact of active material, and structural changes (e.g., K and Mn dissolution). As the cycling proceeds, two important changes are observed in the voltage profiles and long-term cycling performance of the Zn/δ-MnO$_2$ cell: (1) the gradual increase of operating voltages and (2) the capacity fade after cycle 30.

Electrochemical Impedance Spectroscopy. The Nyquist plots for the cycling Zn/δ-MnO$_2$ cell were obtained at several cycling points to grasp more insights on the evolution of voltage and capacity, in particular capacity fade (Figure 3). The variation of impedance (i.e., decrease and increase during cycling) is in agreement with capacity changes (i.e., increase and decrease during cycling) seen in long-term cycling performance (Figures 2c and 3a). The collected and fitted impedance spectra for the first, second, 10th, and 11th cycles (red, orange, dark yellow, and green ones) shows the x-intercept at the highest frequency region and two semicircles at

high and medium frequency region, followed by an inclined (~45°) line at low frequency region that is attributed to Warburg-type impedance of mass transport in a host structure (W_{mt}). The intercept and semicircles are related to an electrolyte resistance (R_e), a passivation layer resistance (R_{pl}-1), and a charge transfer resistance (R_{ct}) (Figure 3c). Accordingly, the fits were performed using Equivalent Circuit 1 shown in Figure 3b. However, the impedance spectra for the subsequent cycles, after the maximum in capacity is reached, can be best represented by the same two semicircles but requires the addition of a semicircle in the medium frequency region followed by Warburg tail at low frequency region to properly model the data (Figure 3d). This additional circuit component models the growth of an additional passivation layer in the system most likely due to electrolyte decomposition (R_{pl}-2 and CPE$_{pl}$-2 in Equivalent Circuit 2 of Figure 3b). Spectral fits revealed that the resistance due to the electrolyte and passivation layer (R_e and R_{pl}-1 in Figure S3a), as well as the capacitance for the passivation layer (CPE$_{pl}$-1 in Figure S3b), were almost unchanged during cycling. However, charge transfer resistance (R_{ct}) decreased and charge transfer capacitance (CPE$_{ct}$) increased up to 30 cycles. This change could be explained by an initial electrochemical grinding, increasing the surface area of active materials. Considering that almost no change was found in the diffusion time constant (Figure S3c), in addition to almost constant electrolyte and passivation resistance during cycling (R_e and R_{pl}-1 in Figure S3a), limited kinetics at the cathode−electrolyte interface induced by the newly formed passivation layer from electrolyte

decomposition could contribute to the gradual capacity fading upon cycling, which will further be investigated below.

Rate Capability. As shown in long-term cycling tests (Figure 2c), the Zn/δ-MnO$_2$ cell delivers a maximum capacity of 123 mAh g^{-1}, while the Coulombic efficiencies remain ≥99.9% even after 125 cycles. With increasing C-rate from C/25 (12.3 mA g^{-1}) to 1C (308 mA g^{-1}) the Zn/δ-MnO$_2$ cell capacity drops from 110 to ~30 mAh g^{-1}, which is recovered when the C-rate was returned to C/25 (Figure 2d). Additional cycles at a current density of C/25 (12.3 mA g^{-1}) shows almost no change in cycling behavior (Figure S4) as that of a typical Zn/δ-MnO$_2$ cell (Figure 2c), which indicates that high C-rate cycling simply increases the charge transfer resistance without damaging the bulk of the material.

Mechanistic Study. *Zn^{2+} Ion Insertion.* Ex situ XRD analysis was conducted for the δ-MnO$_2$ electrodes after the first, second, fifth, and 100th cycles and compared to pristine δ-MnO$_2$ (Figure 4). After the first discharge, the representative δ-

MnO$_2$ peaks, (001) and (002), significantly decrease in intensity especially compared to the mixed indices (11$\bar{1}$) peak. This selective loss suggests a loss of long-range order in the direction of the layers, perhaps due to a structural transformation to another polymorph with similar building blocks but not layered.[29] On subsequent cycles (i.e., the first charge to the second discharge to the second charge to the fifth discharge to the fifth charge) the peak assigned as (11$\bar{1}$) shifts back and forth (Figure 4), indicating a reversible change in unit cell volume in the host material for the charge (Zn^{2+} ion extraction) and discharge (Zn^{2+} ion insertion), respectively. Upon extensive cycling, an additional peak near 34.5° was observed, which can be assigned to the irreversible formation of ZnO. The origin of this phase can be attributed to a few sources including a discharged cathode surface decomposition reaction, an electrolyte salt reaction with water, or a disproportionation reaction of an overzincated material "Zn$_x$MnO$_2$" in the bulk.

By comparing the main edge of the Mn K-edge XANES spectra for three different Mn standard compounds of MnO (Mn^{2+}), Mn$_2$O$_3$ (Mn^{3+}), and MnO$_2$ (Mn^{4+}), it is possible to estimate the redox state of the discharged and charged δ-MnO$_2$ electrodes. Figure 5a shows the direct comparison of Mn standard compounds and pristine/discharged/charged δ-MnO$_2$ samples, while Figure 5b,c represents the spectra of δ-MnO$_2$ samples and Mn standard compounds, respectively. Most importantly, the δ-MnO$_2$ spectra in Figure 5b shifts by a similar amount in energy during discharge and charge, consistent with fully reversible Mn reduction and oxidation during Zn insertion and deinsertion. Note that the initial δ-MnO$_2$ spectrum has the main edge between the Mn$_2$O$_3$ (Mn^{3+}) and MnO$_2$ (Mn^{4+}) standards, which agrees with our elemental and PDF analysis, which showed residual interstitial K$^+$ ions and the presence of bulk manganese vacancies. Intriguingly, the charged sample shifts to higher energy when compared to the pristine sample suggesting that such defect sites may be gradually eliminated upon cycling (Figure 5a,b). Assuming a linear relationship between the absorption edge position and valence (where the average energy shift is defined by five evenly spaced points along the main absorption edge), the pristine Mn oxidation state is 3.6+ and the discharged and charged states are 3.2+ and 3.8+, respectively. These values are approximate since changes in coordination can affect the linear relationship between edge
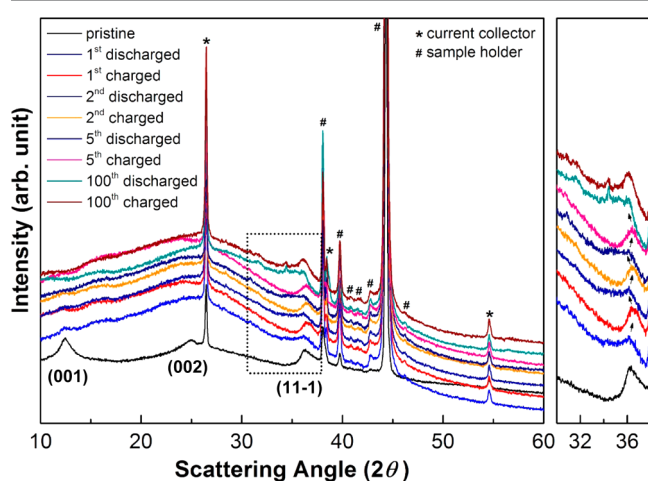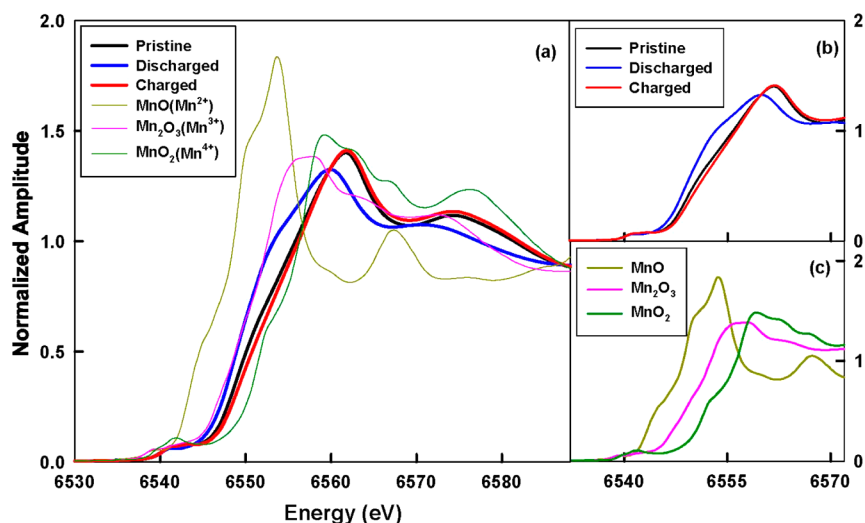

Figure 4. XRD patterns of pristine, discharged, and charged δ-MnO$_2$ electrodes obtained at the first, second, fifth, and 100th cycles. The right magnified figure is corresponding to the dotted rectangle of left figure. The reflections from a current collector (carbon-coated aluminum) and a sample holder were denoted as * and #, respectively.

Figure 5. Mn K-edge XANES for δ-MnO$_2$ samples and different standard compounds of MnO (Mn^{2+}), Mn$_2$O$_3$ (Mn^{3+}), and MnO$_2$ (Mn^{4+}).

shift and valence,[36] but each of these compounds is expected to have octahedrally coordinated Mn sites. Much like the XANES, the local structure of the δ-MnO$_2$ shows reversible changes upon cycling. As shown in Figure S5, the Fourier transformed extended X-ray absorption fine structure (EXAFS) represents a substantial decrease in the first two coordination shells upon discharge and nearly complete recovery upon charge. This significant structural change could be related to Jahn–Teller distortion during reduction to Mn^{3+} upon discharge.

In Figure 6, the characteristic first Mn–O(1) peak (Figure S2)[31,32] in the atomic PDFs subsides (broadens) and reemerges

Figure 6. Atomic PDFs of the pristine, discharged, and charged δ-MnO$_2$ electrodes. The characteristic first Mn–O(1) peak (Figure S2) subsides (broadens) and reemerges (sharpens) upon Zn^{2+} ion insertion and deinsertion.

(sharpens) upon Zn^{2+} ion insertion and deinsertion. These changes are similar to the structural changes one might expect due to breathing modes moving with up and down in magnitude (the EXAFS data in Figure S5), while the average position of Mn–O(1) bond stays almost the same. The minor difference in Mn–O(1) bond lengths of the pristine (1.88 Å) and the charged (1.94 Å) samples is likely attributed to a permanent adjustment of the valence state and the corresponding size of Mn in MnO$_6$ octahedra once it is charged. During the first cycle, the nearly reversible shift (blue and red arrows) of second O(1)–O(1) peak (~2.87 Å) indicates maintenance of the octahedral coordination in the structure by substituting

Mn vacancies with other ions, most likely inserted Zn^{2+} ions, on discharge and relocating some Mn^{2+} ions under the vacancies from deinserted Zn^{2+} ions on charge. In the case of Mn(2)–Mn(2) peak (~4.95 Å), there is no change upon Zn^{2+} ion (de)insertion possibly due to local structural disorder. Compared to back and forth shift of (11$\bar{1}$) peak during cycling in XRD result (Figure 4), the apparent peak shift of an interlayer (~7.52 Å) is not observed as shown in Figure 6.

The ^{1}H NMR spectra normalized to the weight of the samples were plotted and shown in Figure 7. In this experiment a clear peak (2.34 ppm) was observed for the δ-MnO$_2$ electrode samples corresponding to inserted water. For comparison, no proton bearing species were detected in the completely dried (at 120 °C for 24 h) pristine α-MnO$_2$ powder sample that often is observed to be a hydrate indicating the utility the method. The difference between pristine α-MnO$_2$ powder and pristine δ-MnO$_2$ electrode is attributed to the water molecules that were introduced during the synthesis process. On closer inspection of the area between 20 and −5 ppm (Figure 7b) an additional peak at 4.63 ppm emerges and is ascribed to hydroxyl groups (e.g., Zn(OH)$_2$ and MnOOH) that have formed during the electrochemical cycling process. Despite the small peak difference and extra peak, a very low signal-to-noise ratio was observed for all spectra of pristine, discharged, and charged δ-MnO$_2$ electrodes, confirming that the large capacity upon cycles should not be accounted for by proton intercalation. The spectra for the 100 cycled sample shows an increase in the protonic species (Figure S6) compared to those of the first discharged or charged samples, likely due to additional decomposition of an electrolyte and resulting passivation layer on a cathode over extensive cycling. A very minor broad paramagnetic peak is detected within the baseline centered at around 100 ppm, indicative of minor lattice protonation. This is only detected after extensive cycling (not in charged or discharged samples) and thus is not ascribed to the bulk electrochemical activity.

Utilizing a variety of analytical tools, such as ex situ XRD, XAS, PDF, and NMR, the Zn^{2+} ion insertion process in a nonaqueous Zn/δ-MnO$_2$ cell is proposed that it is different from the aqueous Zn/δ-MnO$_2$ studies, which demonstrate a reversible structural transformation between the layered-type δ-MnO$_2$ and spinel-type ZnMn$_2$O$_4$ with Mn(III) state and an intermediary formation of a Mn(II) phase.[16] Previous mechanistic studies of Mg^{2+} ion insertion in birnessite show that intercalation of Mg^{2+} ion takes place in aqueous cells, accompanied by transformation to a spinel-like phase and
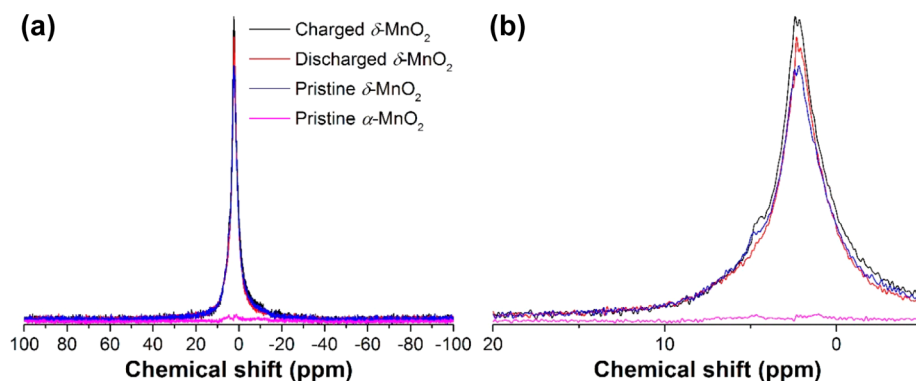

Figure 7. (a) ^{1}H NMR spectra of the pristine, discharged, and charged δ-MnO$_2$ electrodes and completely dried pristine α-MnO$_2$ powders. (b) Zoomed view between 20 and −20 ppm of panel a.
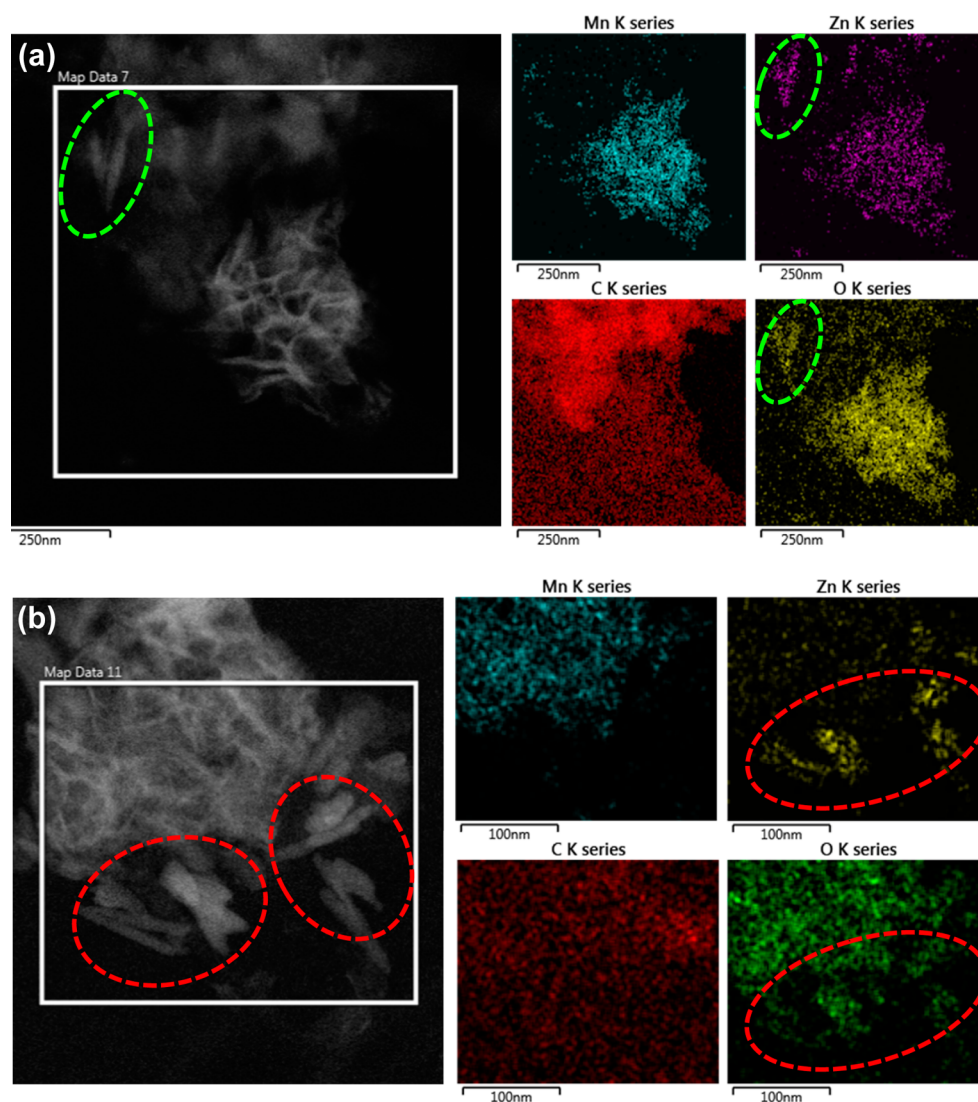
Figure 8. STEM images and element mapping of the selected portion of the second (a) discharged and (b) charged δ-MnO$_2$ electrodes. The ellipsoid parts show regions of Zn and O, which are absent of Mn, further indicating a Zn−oxide formation.

expulsion of interlayer water.[18] It is interesting to note that, however, an irreversible conversion mechanism takes place during cycling in a nonaqueous electrolyte, with the formation of MnOOH, MnO, and Mg(OH)$_2$ upon discharge.[18] In this study, a nonaqueous Zn/δ-MnO$_2$ system demonstrated a reversible Zn^{2+} ion insertion process, albeit with a small amount of ZnO observed on long-term cycling. Several cycled δ-MnO$_2$ cathodes were analyzed using STEM-EDX (Figure 8), and the EDX data acquired shows the apparent formation of ZnO particles in both the discharged and charged samples after the second cycle, respectively. However, the amount of ZnO does not apparently grow on cycling, which may indicate it is not derived exclusively from a lattice breakdown, but may in part come from reactions with water (from initial cathode formulation) or other sources of water or oxide anions (e.g., anode passivation layer) in the cell environment.

Capacity Fading. After the 30th cycle gradual capacity fading is observed (Figure 2c) with increasing impedance (Figure 3a) possibly attributed to either one or a combination of factors, such as decomposition of an electrolyte, slow loss of electronic contact of active material and/or structural changes of a cathode including K and Mn dissolution, or Zn^{2+} ion

impermeable passivation layer formation on a Zn anode. To verify which factors could be leading to the impedance growth in the cell on cycling, additional long-term cycling tests were performed using swapped electrodes. Cells were cycled for 200 cycles, and significant capacity fade was observed. These cells were disassembled and rebuilt with a fresh δ-MnO$_2$ cathode or a fresh Zn anode. The cycled anode is designated 200-Zn and the cycled cathode 200-δ-MnO$_2$. Both sets of cells received fresh electrolyte. In Figure 9a,b, the Zn/200-δ-MnO$_2$ cell has a capacity of ~105 mA g^{-1} after the fifth cycle compared to approximately 60 mAh g^{-1} at the end test from which the electrodes were derived. While the capacity returned, the shape of electrochemical profile was washed out, consistent with structural defects and disorder due to δ-MnO$_2$ losing correlation along the layer axis. However, Figure 9c,d shows the potential profiles and long-term cycling performance of the 200-Zn with a fresh δ-MnO$_2$ cathode. In this case, the cells showed clear plateaus, yet a similar capacity compared to Zn/200-δ-MnO$_2$. From these results, it can be concluded that both electrolyte decomposition and bulk changes in δ-MnO$_2$ on cycling play a role in capacity fading. The later structural
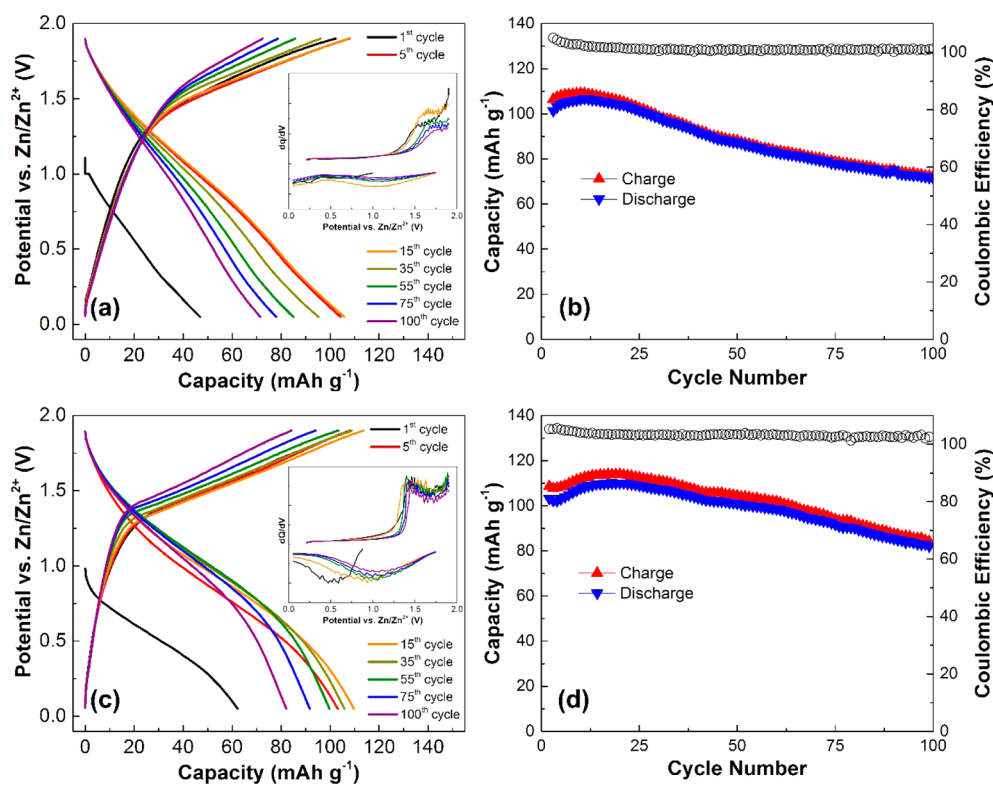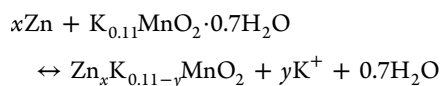
Figure 9. Potential vs capacity profiles (inset: corresponding dQ/dV curves) of (a) a fresh Zn/200 cycled δ-MnO$_2$ cell and (c) a 200 cycled Zn/pristine δ-MnO$_2$ cell, and capacity vs cycle number profiles of (b) a fresh Zn/200 cycled δ-MnO$_2$ cell and (d) a 200 cycled Zn/pristine δ-MnO$_2$ cell in newly prepared 0.5 M AN−Zn(TFSI)$_2$ electrolyte at C/25 C-rates.

changes appear to control the changes in voltage profile and subsequent energy density.

SEM-EDX and ICP-MS analysis of the glass fiber separators collected from a Zn/δ-MnO$_2$ cell without cycling and after 100 cycles revealed a minimal amount of dissolved Mn on the cycled sample (Figure S7). In addition, ICP-MS analysis detected ~28% K and ~6% Mn in the cycled separators based on each amount of K and Mn in as-synthesized δ-MnO$_2$, K$_{0.11}$MnO$_2$·0.7H$_2$O (Figure S8). The detection of K supports our previous suggestion (based on PDFs analysis) that the interlayer K$^+$ ions are released into the electrolyte upon cycles. The increase in Mn concentration is due to minimal dissolution of Mn from δ-MnO$_2$, aggravated by the high surface area of the nanosized active material.[18,33,34]

Based on the observation from (additional) cycling tests, TEM image and element mapping, and ex situ XRD analysis, it can be deduced that the layer-type δ-MnO$_2$ cycles reversibly between the pristine material and Zn$_x$MnO$_2$ (x_{max} = ~0.2 calculated based on the maximum capacity of 123 mAh g^{-1} from Figure 2a) when Zn^{2+} ions insert into the host material upon discharging with a competing side reaction that leads to formation of ZnO (Figure 4). This reaction could be the result of over discharging when the impedance of the cell increased. The overall electrochemical reaction, thus, can be suggested as follows:

$$x\text{Zn} + \text{K}_{0.11}\text{MnO}_2\cdot0.7\text{H}_2\text{O}$$

$$\leftrightarrow \text{Zn}_x\text{K}_{0.11-y}\text{MnO}_2 + y\text{K}^+ + 0.7\text{H}_2\text{O}$$

Subsequent excess charging also results in electrolyte decomposition, as revealed by analysis of the Coulombic efficiency (just slightly below 100%, Figure 2a,c) and

impedance spectra (Figure 3), complemented with experiments where either the electrodes or the electrolyte were replenished in the cell (Figure 9).

CONCLUSIONS

A nanostructured hydrated δ-MnO$_2$ host material with stabilizing bonded water molecules (layered-type birnessite, δ-MnO$_2$) was synthesized to elucidate Zn^{2+} ion insertion mechanism into δ-MnO$_2$ when using a nonaqueous electrolyte system. A nonaqueous Zn metal/δ-MnO$_2$ cell demonstrates good cycling performance that delivers the maximum of 123 mAh g^{-1} capacity at 1.25 V vs Zn/Zn^{2+}. A variety of experimental techniques were used to confirm reversible Zn insertion into the δ-MnO$_2$ host material in a nonaqueous system, without significant proton participation. In contrast, previous studies using an aqueous electrolyte typically have shown that the process of Zn insertion cause structural instabilities for the layered MnO$_2$ host lattice forming other phases (e.g., ZnMn$_2$O$_4$ spinels) and in the Mg/δ-MnO$_2$ system where decomposition to irreversibly form Mg(OH)$_2$ and MgO was observed under nonaqueous conditions. Upon long-term cycling, changes in impedance and capacity fading were attributable to diminished electrolyte performance along with possible competing reactions that result in the precipitation of ZnO on the electrode surfaces and minor amounts of Mn dissolution. Nonaqueous multivalent batteries still have many challenges ahead, but the cycling performance results support the design strategies including nanosizing of active materials, incorporation of water molecules into host crystalline structures, and layered host structure to facilitate multivalent ion intercalation into oxides. In parallel with these design strategies, detailed studies of appropriate materials selection

(for current collectors and cell parts), as shown in recent studies,[37] and cycling conditions optimization are required for the development of multivalent metal batteries.

■ ASSOCIATED CONTENT

ⓢ Supporting Information

The Supporting Information is available free of charge on the ACS Publications website at DOI: 10.1021/acs.chemmater.7b00852.

Supplementary Figures S1–S8 (PDF)

■ AUTHOR INFORMATION

Corresponding Authors
*E-mail: hans@anl.gov.
*E-mail: sanja@anl.gov.
*E-mail: vaughey@anl.gov.

ORCID
Sang-Don Han: 0000-0002-2931-659X
Valeri Petkov: 0000-0002-6392-7589
Jae Jin Kim: 0000-0001-7709-3530
Jordi Cabana: 0000-0002-2353-5986
John T. Vaughey: 0000-0002-2556-6129

Author Contributions

The manuscript was written through contributions of all authors. All authors have given approval to the final version of the manuscript.

Notes

The authors declare no competing financial interest.

■ ACKNOWLEDGMENTS

■ REFERENCES

(1) Muldoon, J.; Bucur, C. B.; Gregory, T. Quest for Nonaqueous Multivalent Secondary Batteries: Magnesium and Beyond. *Chem. Rev.* **2014**, *114*, 11683–11720.

(2) Yoo, H. D.; Shterenberg, I.; Gofer, Y.; Gershinsky, G.; Pour, N.; Aurbach, D. Mg Rechargeable Batteries: an On-Going Challenge. *Energy Environ. Sci.* **2013**, *6*, 2265–2279.

(3) Han, S.-D.; Rajput, N. N.; Qu, X.; Pan, B.; He, M.; Ferrandon, M. S.; Liao, C.; Persson, K. A.; Burrell, A. K. Origin of Electrochemical, Structural and Transport Properties in Non-aqueous Zinc Electrolytes. *ACS Appl. Mater. Interfaces* **2016**, *8*, 3021–3031.

(4) Tutusaus, O.; Mohtadi, R.; Arthur, T. S.; Mizuno, F.; Nelson, E. G.; Sevryugina, Y. V. An Efficient Halogen-Free Electrolyte for Use in Rechargeable Magnesium Batteries. *Angew. Chem., Int. Ed.* **2015**, *54*, 7900–7904.

(5) Rong, Z.; Malik, R.; Canepa, P.; Gautam, G. S.; Liu, M.; Jain, A.; Persson, K.; Ceder, G. Materials Design Rules for Multivalent Ion Mobility in Intercalation Structures. *Chem. Mater.* **2015**, *27*, 6016–6021.

(6) Shannon, R. D. Revised Effective Ionic Radii and Systematic Studies of Interatomic Distances in Halides and Chalcogenides. *Acta Crystallogr., Sect. A: Cryst. Phys., Diffr., Theor. Gen. Crystallogr.* **1976**, *A32*, 751–767.

(7) Zhang, R.; Arthur, T. S.; Ling, C.; Mizuno, F. Manganese Dioxides as Rechargeable Magnesium Battery Cathode; Synthetic Approach to Understand Magnesiation Process. *J. Power Sources* **2015**, *282*, 630–638.

(8) Zhang, R.; Yu, X.; Nam, K.-W.; Ling, C.; Arthur, T. S.; Song, W.; Knapp, A. M.; Ehrlich, S. N.; Yang, X.-Q.; Matsui, M. α-MnO$_2$ as a Cathode Material for Rechargeable Mg Batteries. *Electrochem. Commun.* **2012**, *23*, 110–113.

(9) Novák, P.; Scheifele, W.; Joho, F.; Haas, O. Electrochemical Insertion of Magnesium into Hydrated Vanadium Bronzes. *J. Electrochem. Soc.* **1995**, *142*, 2544–2550.

(10) Novák, P.; Scheifele, W.; Haas, O. Magnesium Insertion Batteries —— an Alternative to Lithium? *J. Power Sources* **1995**, *54*, 479–482.

(11) Gershinsky, G.; Yoo, H. D.; Gofer, Y.; Aurbach, D. Electrochemical and Spectroscopic Analysis of Mg^{2+} Intercalation into Thin Film Electrodes of Layered Oxides: V$_2$O$_5$ and MoO$_3$. *Langmuir* **2013**, *29*, 10964–10972.

(12) Nam, K. W.; Kim, S.; Yang, E.; Jung, Y.; Levi, E.; Aurbach, D.; Choi, J. W. Critical Role of Crystal Water for a Layered Cathode Material in Sodium Ion Batteries. *Chem. Mater.* **2015**, *27*, 3721–3725.

(13) Gautam, G. S.; Canepa, P.; Richards, W. D.; Malik, R.; Ceder, G. Role of Structural H$_2$O in Intercalation Electrodes: The Case of Mg in Nanocrystalline Xerogel-V$_2$O$_5$. *Nano Lett.* **2016**, *16*, 2426–2431.

(14) Bruce, P. G.; Krok, F.; Lightfoot, P.; Nowinski, J. L. Multivalent Cation Intercalation. *Solid State Ionics* **1992**, *53–56*, 351–355.

(15) Senguttuvan, P.; Han, S.-D.; Kim, S.; Lipson, A. L.; Tepavcevic, S.; Fister, T. T.; Bloom, I. D.; Burrell, A. K.; Johnson, C. S. A High Power Rechargeable Nonaqueous Multivalent Zn/V$_2$O$_5$ Battery. *Adv. Energy Mater.* **2016**, *6*, 1600826.

(16) Alfaruqi, M. H.; Gim, J.; Kim, S.; Song, J.; Pham, D. T.; Jo, J.; Xiu, Z.; Mathew, V.; Kim, J. A Layered δ-MnO$_2$ Nanoflake Cathode with High Zinc-Storage Capacities for Eco-Friendly Battery Applications. *Electrochem. Commun.* **2015**, *60*, 121–125.

(17) Nam, K. W.; Kim, S.; Lee, S.; Salama, M.; Shterenberg, I.; Gofer, Y.; Kim, J.-S.; Yang, E.; Park, C. S.; Kim, J.-S.; Lee, S.-S.; Chang, W.-S.; Doo, S.-G.; Jo, Y. N.; Jung, Y.; Aurbach, D.; Choi, J. W. The High Performance of Crystal Water Containing Manganese Birnessite Cathodes for Magnesium Batteries. *Nano Lett.* **2015**, *15*, 4071–4079.

(18) Sun, X.; Duffort, V.; Mehdi, B. L.; Browning, N. D.; Nazar, L. F. Investigation of the Mechanism of Mg Insertion in Birnessite in Nonaqueous and Aqueous Rechargeable Mg-Ion Batteries. *Chem. Mater.* **2016**, *28*, 534–542.

(19) Lee, B.; Yoon, C. S.; Lee, H. R.; Chung, K. Y.; Cho, B. W.; Oh, S. H. Electrochemically-Induced Reversible Transition from the Tunneled to Layered Polymorphs of Manganese Dioxide. *Sci. Rep.* **2015**, *4*, 6066.

(20) Li, D.; Wang, C.; Tripkovic, D.; Sun, S.; Markovic, N. M.; Stamenkovic, V. R. Surfactant Removal for Colloidal Nanoparticles from Solution Synthesis: The Effect on Catalytic Performance. *ACS Catal.* **2012**, *2*, 1358–1362.

(21) Kropf, A. J.; Katsoudas, J.; Chattopadhyay, S.; Shibata, T.; Lang, E. A.; Zyryanov, V. N.; Ravel, B.; McIvor, K.; Kemner, K. M.; Scheckel, K. G.; Bare, S. R.; Terry, J.; Kelly, S. D.; Bunker, B. A.; Segre, C. U.

The New MRCAT (Sector 10) Bending Magnet Beamline at the Advanced Photon Source. *AIP Conf. Proc.* **2009**, *1234*, 299−302.

(22) Newville, M. *IFEFFIT*: Interactive XAFS Analysis and *FEFF* Fitting. *J. Synchrotron Radiat.* **2001**, *8*, 322−324.

(23) Ravel, B.; Newville, M. *ATHENA, ARTEMIS, HEPHAESTUS*: Data Analysis for X-ray Absorption Spectroscopy Using. *J. Synchrotron Radiat.* **2005**, *12*, 537−541.

(24) Petkov, V. *RAD*, a Program for Analysis of X-ray Diffraction Data from Amorphous Materials for Personal Computers. *J. Appl. Crystallogr.* **1989**, *22*, 387−389.

(25) Petkov, V.; Timmons, A.; Camardese, J.; Ren, Y. Li Insertion in Ball-Milled Graphitic Carbons by Total X-ray Diffraction. *J. Phys.: Condens. Matter* **2011**, *23*, 435003.

(26) Gateshki, M.; Hwang, S.-J.; Park, D. H.; Ren, Y.; Petkov, V. Structure of Nanocrystalline Alkali Metal Manganese Oxides by the Atomic Pair Distribution Function Technique. *J. Phys. Chem. B* **2004**, *108*, 14956−14963.

(27) Farrow, C. L.; Juhas, P.; Liu, J. W.; Bryndin, D.; Božin, E. S.; Bloch, J.; Proffen, Th.; Billinge, S. J. L. PDFfit2 and PDFgui: Computer Programs for Studying Nanostructure in Crystals. *J. Phys.: Condens. Matter* **2007**, *19*, 335219.

(28) Holland, K. L.; Walker, J. R. Crystal Structure Modeling of a Highly Disordered Potassium Birnessite. *Clays Clay Miner.* **1996**, *44*, 744−748.

(29) Luo, J.; Zhang, Q.; Suib, S. L. Mechanistic and Kinetic Studies of Crystallization of Birnessite. *Inorg. Chem.* **2000**, *39*, 741−747.

(30) Thackeray, M. M. Manganese Oxides for Lithium Batteries. *Prog. Solid State Chem.* **1997**, *25*, 1−71.

(31) Petkov, V. Nanostructure by High-Energy X-ray Diffraction. *Mater. Today* **2008**, *11*, 28−38.

(32) Petkov, V.; Ren, Y.; Saratovsky, I.; Pastén, P.; Gurr, S. J.; Hayward, M. A.; Poeppelmeier, K. R.; Gaillard, J.-F. Atomic-Scale Structure of Biogenic Materials by Total X-ray Diffraction: A Study of Bacterial and Fungal MnO_x. *ACS Nano* **2009**, *3*, 441−445.

(33) Delmas, C.; Cognac-Auradou, H.; Cocciantelli, J. M.; Ménétrier, M.; Doumerc, J. P. The $Li_xV_2O_5$ System: An Overview of the Structure Modifications Induced by the Lithium Intercalation. *Solid State Ionics* **1994**, *69*, 257−264.

(34) Li, H.-Y.; Yang, C.-H.; Tseng, C.-M.; Lee, S.-W.; Yang, C.-C.; Wu, T.-Y.; Chang, J.-K. Electrochemically grown nanocrystalline V2O5 as high-performance cathode for sodium-ion batteries. *J. Power Sources* **2015**, *285*, 418−424.

(35) Sa, N.; Kinnibrugh, T. L.; Wang, H.; Sai Gautam, G.; Chapman, K. W.; Vaughey, J. T.; Key, B.; Fister, T. T.; Freeland, J. W.; Proffit, D. L.; Chupas, P. J.; Ceder, G.; Bareno, J. G.; Bloom, I. D.; Burrell, A. K. Structural Evolution of Reversible Mg Insertion into a Bilayer Structure of $V_2O_5 \cdot nH_2O$ Xerogel Material. *Chem. Mater.* **2016**, *28*, 2962−2969.

(36) García, J.; Subías, G.; Cuartero, V.; Herrero-Martin, J. On the correlation between the X-ray absorption chemical shift and the formal valence state in mixed-valence manganites. *J. Synchrotron Radiat.* **2010**, *17*, 386−392.

(37) Lipson, A. L.; Han, S.-D.; Pan, B.; See, K. A.; Gewirth, A. A.; Liao, C.; Vaughey, J. T.; Ingram, B. J. Practical Stability Limits of Magnesium Electrolytes. *J. Electrochem. Soc.* **2016**, *163*, A2253−A2257.